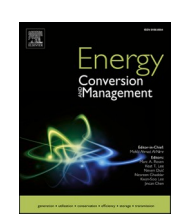
ELSEVIER

Contents lists available at ScienceDirect

Energy Conversion and Management

journal homepage: www.elsevier.com/locate/enconman





Shifting to energy efficient hybrid cooled data centers using novel embedded floor tiles heat exchangers

Yaman M. Manaserh ^{a,*}, Mohammad I. Tradat ^a, Ahmad R. Gharaibeh ^a, Bahgat G. Sammakia ^a, Russ Tipton ^b

^a Department of Mechanical Engineering, ES2 Center, Binghamton University-SUNY, NY, USA

ARTICLE INFO

Keywords:
Data center
Liquid cooling
CFD modelling
Energy efficiency
Thermal management
Hybrid Cooling

ABSTRACT

With the remarkable surge in IT power densities and energy consumption, the data center industry is starting to adopt energy and thermally-efficient single-phase cooling technologies. For many legacy data centers worldwide, the lack of a primary chilled water source is a substantial barrier to adopting single-phase technologies. In this study, the necessity of having a facility chilled water source for deploying liquid cooling solutions is eliminated by introducing a solution that does not require bringing in any modification of the data center layout. This simple solution proposes integrating liquid to air heat exchangers with the floor tiles to eject heat from the liquid-cooled IT equipment into the room air. An experimentally validated CFD modeling approach is used to investigate the performance of these heat exchangers. Results show that by installing two heat exchangers in different cold aisles, a significant amount of cooling load is handled at the design point conditions. When they are tested under different operational conditions, the cooling capacity of these heat exchangers is shown to be sensitive to the supply air temperature. To overcome the operational constraints stemming from the supply air temperature, an alternative configuration with just one heat exchanger installed in the hot aisle is considered and discussed. Results indicate that the second configuration shows superior performance to the first one in terms of sensitivity to supply air temperature and cooling capacity. Lastly, with this configuration, the data center utilizes energy extremely efficiently and achieves a power usage effectiveness of 1.06.

1. Introduction

Stabilizing Earth's temperature by reducing greenhouse emissions has become a mission-critical task for many governments around the world [1]. Accordingly, this has pushed many industries to reduce their energy consumption and adopt more energy-efficient solutions [2,3]. One of these industries is Data Centers (DCs). DCs are energy-intensive enterprises that accounted for 2% [4] of the total United States electricity usage and 1.5% [5] of worldwide usage in 2012 and 2011, respectively. By 2020, worldwide usage was expected to rise to 8% [6], accounting for 4% of total global emissions [7]. DCs are the backbone of the digitalized world. Their energy consumption is expected to further increase due to the emergence of data-intensive technologies, such as artificial intelligence, image processing, machine learning, and internet usage [8]. This demand is forecasted to grow by 15–20% annually [9]. In DC infrastructure, cooling systems are responsible for 30–50% of energy consumption [10–12]. In addition, it has been found that more than 50%

On the component level, H. Saber et al. [14] conducted an optimization study to minimize the chip temperature non-uniformity, and its power consumptions. B. Kanargi et al. [15] carried out a comprehensive investigation on an oblique finned- heat sink cooled by air, the study considered two oblique angles 30° and 45° .

W. Zhou et al. [16] developed a woven mesh wick to improve the thermal performance of an ultra-thin heat pipe that was designed to be used in cooling electronic devices. N. Gilmore et al. [17] introduced a new open manifold microchannel for cooling electronics. The authors found that by adopting such a solution, the pressure dropped by 25% without changing the thermal performance, which is expected to result in huge energy savings at the data center level. On the DC level, Q. Pan et al. [18] investigated using an adsorption refrigeration system for

E-mail address: yyaseen1@binghamton.edu (Y.M. Manaserh).

0196-8904/© 2021 Elsevier Ltd. All rights reserved.

b VERTIV, Columbus, OH, USA

of DCs' cooling systems are inefficient [13]. These facts have prompted investigations into reliability concerns, potential solutions, energy-saving opportunities, the adoption of new cooling technologies, and the integration of renewable energy in the DC research field. More indepth studies are introduced below:

^{*} Corresponding author.

recovering waste heat in data centers. B. Fakhim et al. [19] studied a few designs and solutions including different Computer Room Air Conditioning (CRAC's) installations, using containment for the cold aisle, and adopting a ceiling return air distribution system to improve the performance of the cooling system. J. Cho and Y. Kim [20] evaluated the DC energy usage by studying placing the impact of placing the data centers in various geographical regions and adopting different cooling systems. They considered four locations and examined energy consumption using an energy model tool. Their results revealed that the DC's energy performance was highly affected by its geographical location and the adopted cooling system. H. Chen et al. [21] Proposed a hybrid cooling system to be used during off-peak time to supplement the cooling system when the IT equipment load reaches its peak value. H. Moazamigoodarzi et al. [22] compared different data center cooling architectures considering room-based architecture, row-based architecture, and rackbased in terms of DC energy efficiency. Their analysis showed that the cooling power can be reduced by as much as 29% in the case of replacing the room-based architecture with row- and rack-based architectures. M. T-Evans et al. [23] carried out a study to investigate the effect of cold air bypassing the ITE on the DC's energy consumption. J. Li et al. [24] proposed a new indicator referred to as the coefficient of power usage effectiveness (COPUE) for a fair comparison in terms of energy performance between DCs operating under different climatic conditions. Z. Song et al. [25] used a Genetic Algorithm along with neural networks to optimize the airflow and temperature distribution to reduce energy usage in DCs. W-X Chu and C-C Wang [24] provided a review on airflow management in DCs. In their study, DCs were categorized according to the available airflow path, and cooling systems as either long or shortdistance cooling systems. The aforementioned research papers focused mainly on air-cooled DCs.

Air cooling is the most durable, and widely used technique for cooling electronics [26]. However, the constant growth in energy demand and the ever-increasing heat generated over a smaller area of electronic equipment are driving factors that necessitate the need of boosting the air technologies' cooling limits. One solution is to adopt air-assisted liquid cooling, by doing so, the life of existing air-cooled facilities can be extended, and a smooth transition between fully air-cooled data centers to fully liquid-cooled data centers can be achieved. According to the extensive investigations carried out by literature [27–29],

single-phase liquid cooling techniques are recognized as effective, energy-efficient, and feasible when it comes to cooling electronics with high heat flux density. With regard to DC facility-level liquid cooling studies, S. Zimmermann et al. [30] used the experimental results from a DC prototype called Aquasar to demonstrate that hot water can be used as a coolant to meet the cooling requirements of DCs. Moreover, the authors expressed that reusing warm water for space heating can recover up to 80% of the DC waste heat. A. Carbó et al. [31] developed a dynamic model to study the energy usage of liquid-cooled DC. T. Gao et al. [32] provided a dynamic response of each component in a liquid-cooled chiller-less DC using test and simulation results. The IBM team [33] characterized the performance of a warm water-cooled DC. They found that by rejecting the heat to ambient air, they were able to reduce the energy consumption of the cooling system to 3.5% of the total IT energy consumption.

Currently, liquid cooling solutions are being widely integrated into modern High-Performance Computer systems [34]. When installed in DCs, these solutions use fluid to remove heat from the ITE and eject it into the facility's chilled water source through an external cooling distribution unit. Thus, with the absence of a primary water-cooled loop, the adoption of liquid cooling solutions is impossible, unless the heat is dissipated to the data center space. The problem with many legacy-raised floors and air-cooled DCs, which constitute the preponderance of existing DCs, is that they were designed to be purely air-cooled. Therefore, a chilled water source might not be feasible or accessible, and in some cases, it does not exist based on the facility design. Redesigning or replumbing these DCs to bring in primary chilled water sources worldwide would require investing billions of dollars, which for some small-scale DCs is a cost that they cannot afford.

In this study, a novel solution is proposed to help implement liquid cooling systems and to assess the sustainability of legacy raised floor DCs with limited or no access to facility chilled water. The solution doubles the utilization of the data center floor tiles by embedding a liquid to air HX within the perforated floor tiles, thereby allowing the cold air supplied by the unit to absorb the heat from the coolant of the liquid-cooled ITE before it enters the DC space. According to the design of these HXs, they would be extremely easy to adopt without imposing any modification to the data center layout and can be resized to fit in any data center starting from a one-aisle data center to a mega-scale data center.

Previous research has broadly studied thermal management in aircooled DCs and has presented many solutions for improving cooling system performance. For liquid-cooled solutions, a relatively small number of papers discuss liquid cooling implementation at the facility level, instead, most focus on the component level. To the best of the authors' knowledge, this type of liquid to air HX has never been introduced or discussed in the literature before, whether it was embedded in the floor tiles or installed as a split unit. The novelty of this paper is that it proposes a new, reliable, effective, and energy-efficient solution to facilitate implementing liquid cooling in existing legacy air-cooled DCs using a HX embedded in the floor tiles. The goal of this paper is to verify the feasibility and effectiveness of this solution in the thermal environment of a raised floor DC. The functionality of this solution was ascertained via simulations using a validated CFD model. Moreover, these simulations are extended further to provide a more thorough investigation of hybrid cooled DC operation. This helps to fill an essential knowledge gap in the research literature, seeing as hybrid cooling is expected to be the future of data center cooling. Hence, this paper would provide fertile soil for the new field of hybrid cooling research in the data center industry.

With the DC industry in transition and the search for alternatives to air cooling ongoing, the embedded floor HX presented in this work comes at a critical time. Thus, according to their huge cooling capacity, they could establish a new concept of data centers that utilizes an energy-efficient hybrid cooling system. Hence, this solution could change the perspective of adopting liquid cooling techniques in data centers because it proposes a methodology that does not require facility chilled water.

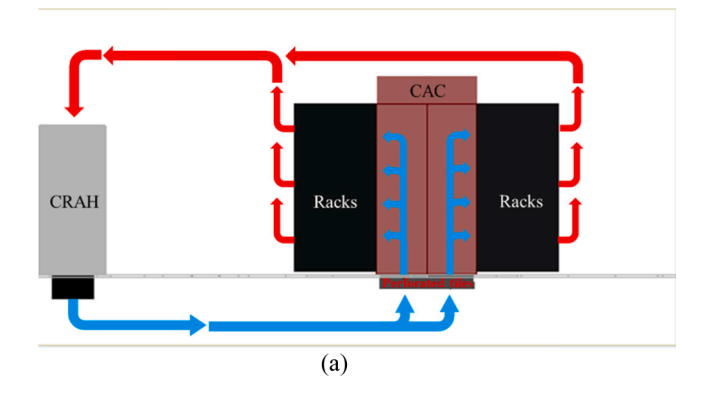
Hereafter, the paper is structured as follows: The CFD model design is described, including details of the facility, governing equations and turbulence model, grid generation, model validation, and experimental setup, and the HX model. Then, the numerical results are discussed considering three different aspects, namely the solution's design limitations, the effect of the DC operational conditions on the proposed system's performance, and an alternative configuration for the proposed system. Finally, further conclusions are provided in the last section.

2. Methodology (simulation solution)

2.1. Background and concept description

Legacy-raised floor and air-cooled DCs, like the one shown in Fig. 1 (a), constitute the preponderance of existing DCs. Generally, their cold air is supplied by the CRAC or Computer Room Air Handler (CRAH) unit (s) through the pressurized underfloor plenum. Thereafter, the cold air is distributed to the cold aisle through perforated floor tiles and enters the ITE. Inside the ITE, the cold air absorbs heat from its component before being drained into the hot aisle by the ITE fans. Finally, the hot air returns to the cooling unit(s) and cools down again.

With the remarkable increase in the heat generated by electronic devices, liquid cooling solutions are being more widely implemented in DCs. When implemented, liquid cooling can take on many forms. The most common one utilizes a liquid to liquid HX called a Cooling Distribution Unit (CDU) to transfer the heat from coolant in the ITE cooling system to the facility water system [35]. The CDU can be assigned to a single rack by installing it within the rack, or it can be allocated to feed multiple racks by installing it as an external unit. CDU(s) are multipurpose, most often used to separate various ITE coolants from the facility water, facilitate circulation, maintain high-quality coolant, and control the coolant temperature. Fig. 1 (b) depicts a liquid cooling configuration that uses an external CDU in a DC. Currently, cold plates (indirect single phase) are the most widespread liquid cooling apparatus in the electronics cooling industry [36-38]. These cold plates are attached to the high-power dissipation components inside the ITE, such as CPUs and GPUs, to pick up heat from these components. These cold plates are designed and built through advanced manufacturing methods



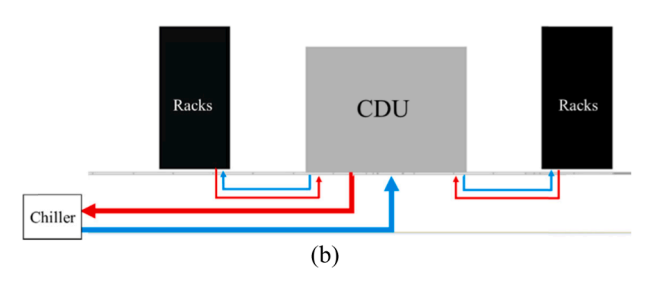


Fig. 1. Typical configuration of raised floor air and liquid-cooled DCs (a) air-cooled DC (b) liquid-cooled DC.

to maximize the use of liquid coolants' heat capacity. Even so, unless the ITE is fully immersed in coolant, air cooling techniques must still be used to extract the heat dissipated by other ITE components, like the Random-Access Memory (RAM), power supply, and Hard Disk Drives (HDD) [39].

As mentioned, one of the primary barriers to implementing liquid cooling in many legacy air-cooled DCs is the availability or feasibility of a chilled water source. For some, there simply is no chilled water source sufficient to remove the ITE heat. For others, there is a chilled water source but with limited or no accessibility, which would require DC redesign or replumbing. In light of this, liquid to air cooling distribution units can be used to circumvent the need for facility chilled water while also tapping into the advantages of liquid cooling. Essentially, these units utilize pumps to circulate coolant between the ITE and the HX coil, while also using fans to draw air from the cold aisle, which will be used to cool the fluid while it is in the HX coil. An example of this

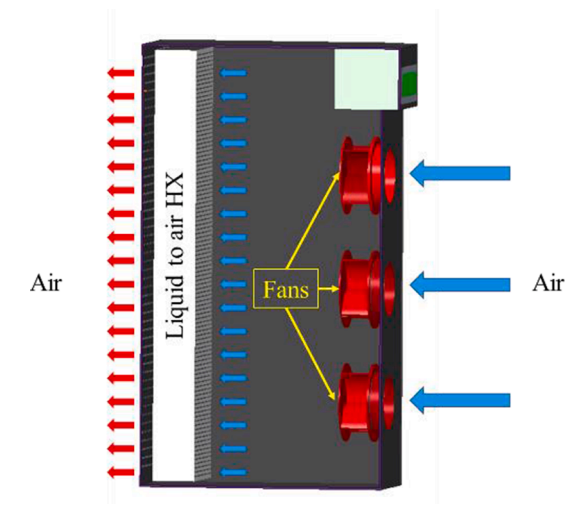


Fig. 2. Cooling distribution unit with liquid to air HX.

configuration is shown in Fig. 2. However, these cooling units have some drawbacks which can be summarized as follows: (1) They require a significant amount of air that must be delivered to the cooling unit with exactitude, which might be difficult to do (2) They utilize relatively large fans to push air through the HXs, which consumes a considerable amount of energy (3) The high temperature of the air-jet exiting this type of unit might be hazardous to other ITE (4) This unit will compete with adjacent ITE for the cool air supply, which could create hot spots therein (5) Seeing as this unit must be installed close to the liquid-cooled rack(s), modifications to the DC layout might become necessary. These observations were made based on experimental investigations, technical manuals [40], and research articles that discuss the environments of data centers [41,42].

In this work, the authors propose embedding the HX within the perforated floor tiles. With this setup, the HX is connected to a row manifold that circulates coolant between the liquid-cooled racks and the HX. Fig. 3 (a) demonstrates the liquid coolant cycle in this system. The coolant enters the ITE and engulfs the heat generated from a specific component within it for example the CPU, then it returns to the rack manifold, which delivers the coolant to the row manifold. Row manifold collects the heated coolant from different rack manifolds and supplies it to the HX embedded in the floor tiles, shown in Fig. 3 (b-d). As the plenum cold air passes through the HX, it extracts heat from the coolant,

and then the coolant returns to the row manifold to be distributed to the rack manifolds.

The existing plenum pressure is responsible for pushing the cold air across the HX. Having the HX embedded in the floor tiles provides passive cooling since the airflow through it is not mechanically driven. Instead, it relies on the pressure difference between the underfloor plenum and cold aisle containment (CAC). Compared with the conventional liquid to air HX solution, which utilizes relatively large fans to drive air through the HX, this setup can potentially save a significant amount of energy. In a mega-scale data center, we might need tens or even hundreds for operating such a data center also these units are expected to operate 24/7, in such cases, enormous savings could be achieved. Annual savings were calculated and provided in Appendix A. These savings by assuming that the unit consumes 3 kW and the electricity price is \$0.1319 per kilowatt-hour (kWh).

This system utilizes air to deploy liquid cooling technology to efficiently cool the ITE high-power density components and at the same time, air will be used for cooling other components within the server. Where the liquid will be picking up the heat from the high-power density components such as CPUs and GPUs using liquid-cooled heat sinks, while air will be picking up the heat from low power density components such HDDs and RAMs. Even though the proposed cooling system is solely utilizing the CRAH units as the sole cooling source, the hybrid

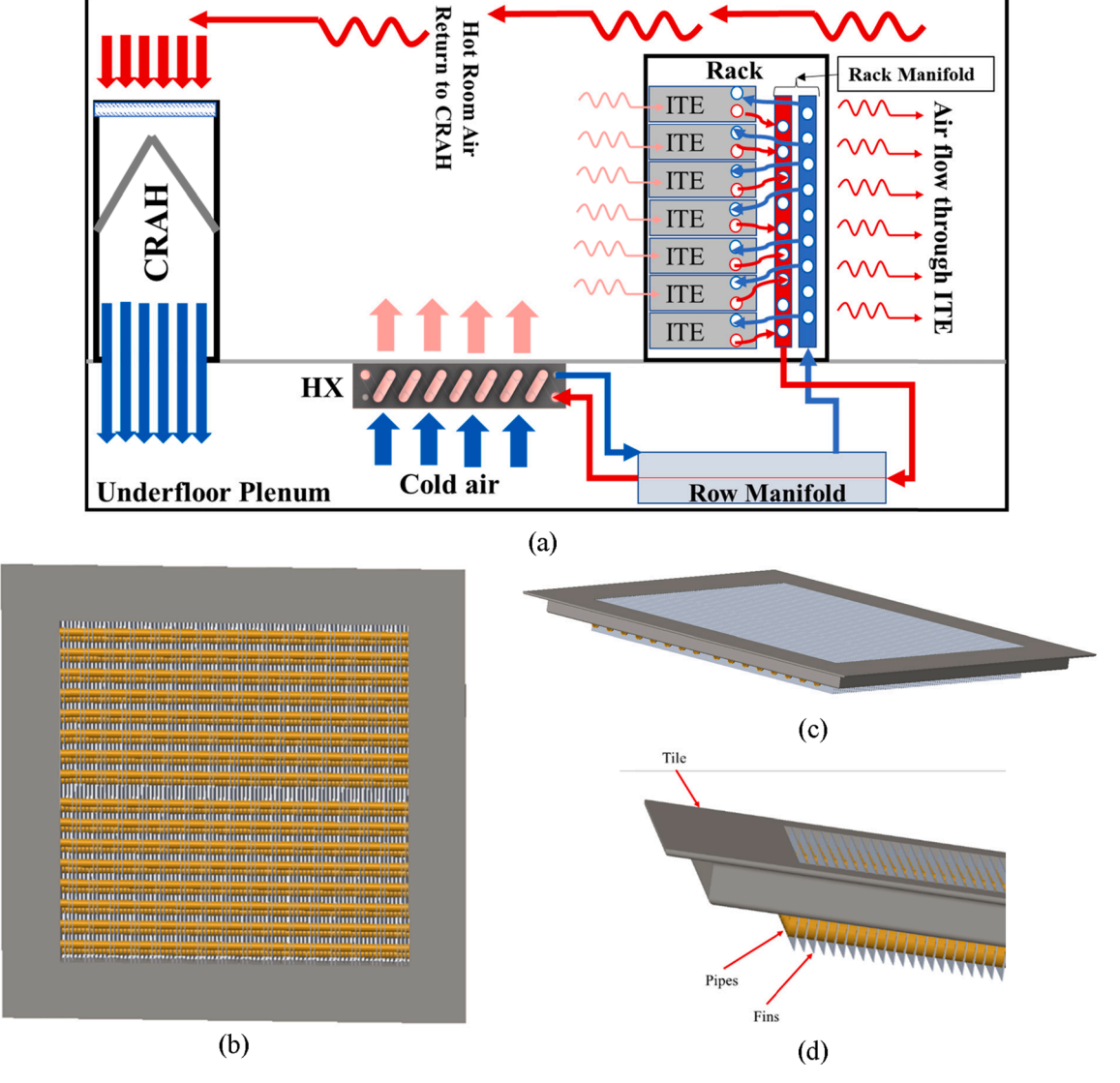


Fig. 3. Proposed system (a) cooling cycle (b-d) CAD drawing of the perforated tiles integrated with liquid to air HX.

cooling term was adopted considering the fact that ITE is cooled by both air and water at the same time.

2.2. Numerical model

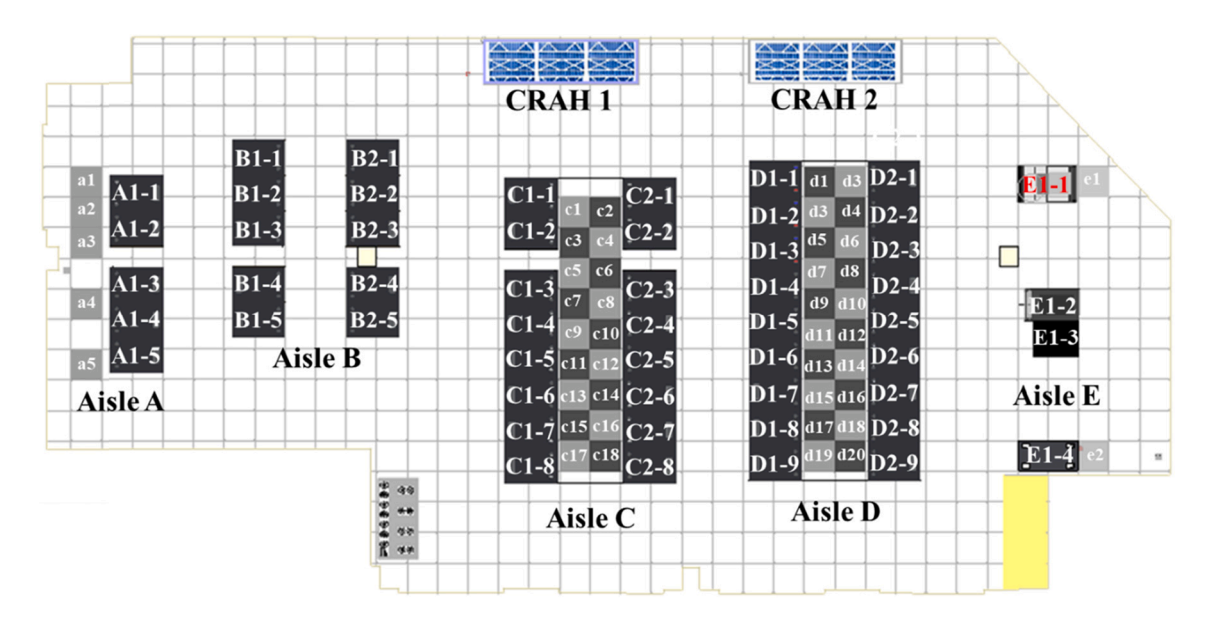
Over time, researchers have continued to utilize CFD techniques, which have become even more important because of their reliability with characterizing and improving systems. In fact, CFD tools have become an inextricable part of the design and development stage of electronics cooling. This is attributed to the huge amount of time and effort that they can save, and their capability to precisely predict the thermal performance of electronics. In this work, a commercial CFD code of 6sigmaroom was used to build a digital twin of the Energy-Smart Electronics System (ES2) DC at the State University of New York at Binghamton and to conduct simulations. The reason being that this code specializes in running simulation at the DC facility level and has shown it can produce reliable results in the literature [42–44].

• Data center facility description

The ES2 research DC is a raised floor DC that consists of five aisles with a traditional hot aisle/cold aisle arrangement. These aisles are named as follows: A, B, C, D, and E, where Aisles B and E are currently off duty. Aisle A has one row of racks, while aisles C and D have two rows of racks enclosing the cold aisle. The aisle pitch, which is the distance between two cold aisle centers, varies between 4.27 and 5.49 m. This DC is thermally managed by two CRAH units that control the flow rate utilizing a variable frequency drive. The ES2 DC map view and aisles configurations are illustrated in Fig. 4, while Table 1 summarizes additional information regarding the data center's specifications.

Like many other DCs, the rack power density varies within the DC. Moreover, the open area ratio is heterogeneous throughout the DC. The racks' power density and the openness of perforated tile openness considering each aisle are introduced in [12]. It can be noted from the appendix provided in this manuscript that the open area ratio between the perforated tiles deviates significantly which explains the considerable variation in the flowrate delivery for each tile.

• Governing equations and turbulence model



(a)



(b)

Fig. 4. ES2 DC (a) Schematic view (b) actual DC.

Table 1 ES2 DC specifications.

Items	Description	Value
Room	Area (m^2)	215.75
	Height (m)	4.37
	Raised floor height (m)	0.914
	Perforated Tiles number	45
	Dimensions of the perforated tile (m)	(0.61×0.61)
	Total racks number	53
	Total racks load (kW)	120
CRAHs	CRAH units number	2
	Total cooling capacity of the CARH units (kW)	399
	Maximum airflow rate of CRAH 1 (m^3 . s^{-1})	7.79
	Maximum airflow rate of CRAH 2 (m^3 . s^{-1})	8.165

This CFD code is a finite volume-based code and has a 3D solver for the conservation of mass, momentum, and energy equations:

$$\frac{\partial \rho}{\partial t} + \frac{\partial (\rho u_i)}{\partial x_i} = 0 \tag{1}$$

$$\frac{\partial(\rho u_i)}{\partial t} + \frac{\partial(\rho u_i u_j)}{\partial x_j} = -\frac{\partial P}{\partial x_i} + \frac{\partial \tau_{ij}}{\partial x_j} + F_i$$
(2)

$$\frac{\partial(\rho E)}{\partial t} + \frac{\partial(u_m(\rho E + P))}{\partial x_m} = \frac{\partial}{\partial x_j} \left(k_{eff} \frac{\partial T}{\partial x_j} \right) + \Phi + S$$
(3)

where, τ_{ij} represents the stress tensor, F_i denotes the body forces, S denotes the volumetric heat generation, and Φ represents the dissipation function.

Generally, the flow dynamics of DCSs are very complicated, and numerous vortices can develop [45]. Based on this, Reynolds Averaged Navier-Stokes (RANS) was considered to close Navier-Stokes and Reynolds stress equations. According to the literature [46,47], standard k- ϵ is a feasible turbulence model for simulating the flow in DCs, and therefore is adopted in this work. The standard k- ϵ governing equations are provided below [48–50]:

$$\frac{\partial(\rho k)}{\partial t} + \frac{\partial(\rho k u_i)}{\partial x_i} = \frac{\partial}{\partial x_i} \left[\left(\mu + \frac{\mu_t}{\sigma_k} \right) \frac{\partial k}{\partial x_j} \right] + G_k + G_b - \rho \varepsilon - Y_M + S_K$$
 (4)

$$\frac{\partial(\rho\varepsilon)}{\partial t} + \frac{\partial(\rho\varepsilon u_i)}{\partial x_i} = \frac{\partial}{\partial x_j} \left[\left(\mu + \frac{\mu_t}{\sigma_{\varepsilon}} \right) \frac{\partial\varepsilon}{\partial x_j} \right] + C_{1\varepsilon} \frac{\varepsilon}{k} (G_k + C_{3\varepsilon} G_b) - \rho C_{2\varepsilon} \frac{\varepsilon^2}{k} + S_{\varepsilon}$$
(5)

The turbulent viscosity is defined as:

$$\mu_t = \rho C_\mu \frac{k^2}{c} \tag{6}$$

A detailed description of the standard k- ϵ governing equations can be found in [12]. However, the following are the assumptions made during simulation:

- 1. Air is incompressible and has constant properties.
- 2. The system operates at steady-state conditions.
- 3. Gravity and wall roughness are negligible.
- 4. The outer walls, including the floor and ceiling, are adiabatic.
- 5. The DC cooling units' capacity is infinite.

The last assumption was made to isolate the cooling capacity of the embedded floor tile HX by avoiding potential limitations presented by the cooling units.

• Grid method

The grid method, also known as the generation of the mesh, plays a critical role in determining the accuracy of numerical model outputs.

Hence, a convenient grid quantity and quality should be guaranteed when constructing the grid. A structured hex mesh was used to build the model grid. The advantage of cubic hex cells is they ensure the grid quality and can overcome the aspect ratio and skewness issue that commonly occurs when using a tetrahedral mesh [51]. The maximum grid aspect ratio was limited to 3 while the maximum grid expansion ratio (i.e. size ratio between adjacent cells) was restricted to no greater than 2.

A grid sensitivity study was carried out to meet the requirements of computational accuracy and to remove the influence of the grid number on the results. The grid independence study was inaugurated by deploying a relatively small number of grids, which was then gradually increased. In order to strike a balance between computing expense and accuracy, the results were scanned to detect the point at which further increment in the grid number induced minimal variation in the temperature and flowrate results. The grid independence study was conducted over five mesh groups, the grid number was chosen to be 8.5 $\times 10^6$ according to Fig. 5, which shows that the results for the average tile flow delivery in both aisles as well as C1-2 and D1-3 temperature sensors (shown in Fig. 6) are stabilizing at this specific value.

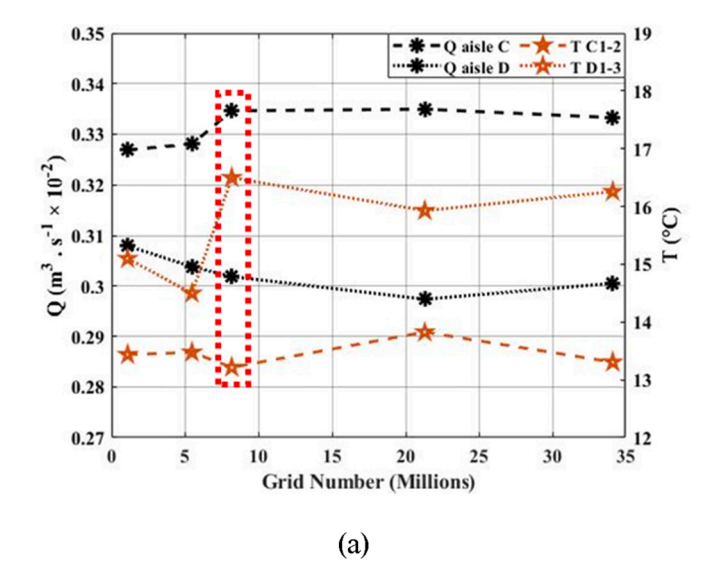
• Model validation and experiment description

To ascertain the CFD model's accuracy, a validation study was conducted utilizing the experimental results. The experimental measurements were recorded in the DC. Then, the CFD model was synchronized to replicate the exact same operating conditions as in the experiment. In the experiment, a total of eight temperature sensors were used to collect temperature measurements, with four in each aisle, which supplemented the CRAH unit return air temperature readings. These sensors were installed at the rack inlets, $1.9\ m$ above the raised floor. Moreover, six pressure sensors were placed in aisles C and D, $2\ m$ above the raised floor. Temperature and pressure sensor locations are shown in Fig. 6, where temperature sensors are shown in yellow and pressure sensors are shown in blue. Sensors were named according to the rack on which they were installed.

An ADM-850 L multimeter flow hood was utilized to report airflow measurements through each aisle. This flow hood has an accuracy of \pm 3% according to the vendor's technical manual. A fine-grain wireless sensing technology called SynapSense was used to obtain temperature readings at different locations within the DC. As mentioned, the CRAH's built-in sensors reported the CRAH return air temperature readings. Finally, Bapi ZPT-LR pressure sensors were used to quantify the pressure readings inside the under-floor plenum and the CAC. These sensors have a range of 0–249 Pa and an accuracy of \pm 0.25% of the full range which equals 0.625 Pa. Fig. 7 shows the instrumentation used in this study.

The experiment was conducted as follows. First, the cooling units were adjusted using the building's thermal management system provided by Siemens. Thereafter, the racks' temperature sensor readings and the air temperature returning to the CRAH units were monitored to assure steady state was achieved. Only temperature measurements were considered since temperature fields take a substantially longer time than pressure and flow fields to reach steady-state within DCs. When steady-state conditions were achieved, the temperature measurements were automatically collected using the SynapSense website, the pressure sensors readings were acquired through the Keysight 34980A switch and measure unit, and the tiles' flowrate measurements were manually taken using the flow hood. To ensure the reliability of the flowrate results, five measurements were taken for each tile and the average value was reported.

In the numerical part, pressure and temperature sensors were created and placed in the same spatial location as in the experimental setup. The following boundary conditions were imported to the CFD model from the experiment. CRAH 1 supplied air at a temperature of 10.4 $^{\circ}$ C with a speed of 70%, while CRAH 2 supplied air at a temperature of 15.8 $^{\circ}$ C



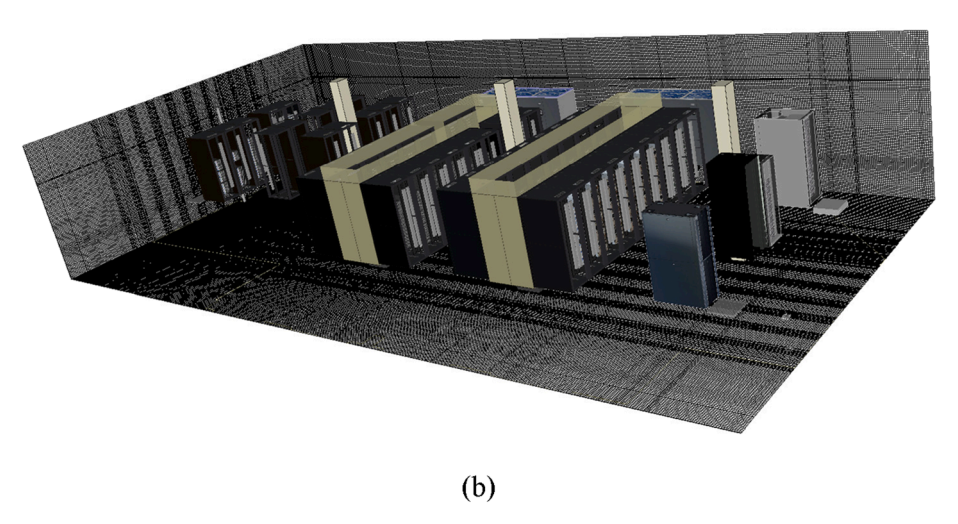


Fig. 5. CFD model grid generation (a) Grid sensitivity analysis (b) model generated grid.

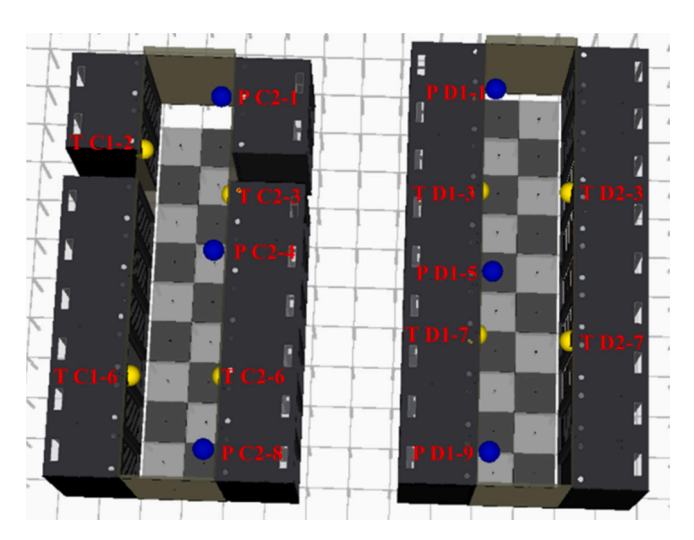


Fig. 6. Sensors placement in aisles C and D.

with a speed of 100%. Each rack's power consumption was reported and integrated into the CFD model as a boundary condition. This data was gathered from the racks' power distribution units.

A comparison of the numerical results and the field measurements is illustrated in Fig. 8. It can be noted that there is great consistency between the experimental measurements and the numerical simulation results. The numerical results for average airflow delivery were within one standard deviation from the experimental measurements. The temperature distribution from the numerical results was almost the same as that from the field measurements. The maximum deviation between the temperature sensor readings and the numerical results was 1.65 °C, at rack D2-3. The CRAH units' return air temperature mismatch between the experimental and numerical results was 0.07 °C and 0.87 °C for CRAH 1 and CRAH 2, respectively. The highest temperature field measurement standard deviation was found to be equal to 0.12, hence error bars are not plotted in Fig. 8 (c). Lastly, the numerical result for the pressure field matched the field measurement. The maximum difference in the pressure readings was 0.8 Pa. This reading was provided by the sensor located at rack D1-5. It is worth mentioning that the pressure sensor readings fluctuated during the experiment with an average range of 2 Pa.

In real world, due to the dynamic nature of the data center environment, it is extremely hard to achieve steady-state conditions, thus the

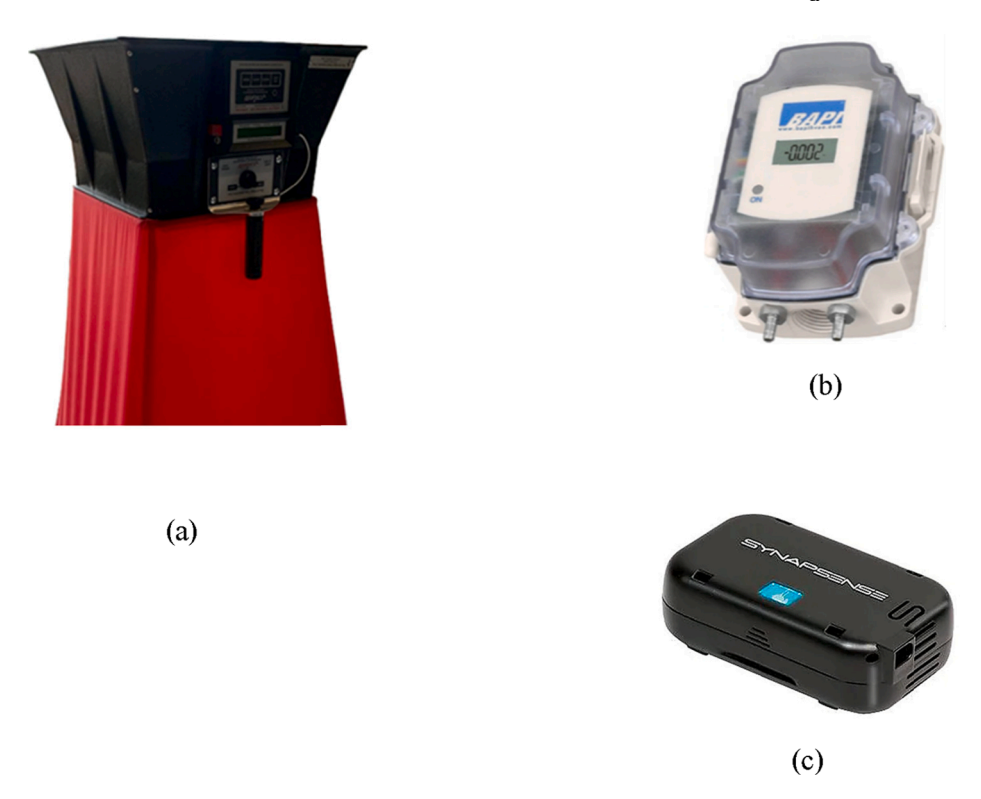


Fig. 7. Instrumentation used in the validation experiment (a) flow hood (b) pressure sensor (c) temperature sensor.

sensors keep exhibiting small variations in their measurements. Moreover, the sensors themselves have their own accuracy and stability, which is another source of error in the measurements. Based on the above and the fact CFD is a numerical technique that assumes a steady state is truly achieved, it is expected that there would a small mismatch between the experimental data and the CFD one. Since that the CFD results lie within one standard deviation and within the sensor accuracy, this means that the CFD model predicts the data center performance. Accordingly, the overall results validate the feasibility and reliability of the CFD model applied in this work.

2.3. Heat exchanger modeling

In this CFD code, the HX object is represented by a simplified black-box model, where the HX's air resistance is calculated by defining the construction of its circuits and fins. The choice of an effectiveness or conductance curve can be used to define the performance specifications of the HX. In this study, the conductance curve approach was adopted and calculated using:

Thermal Conductance =
$$hA$$
 (7)

Typically, the heat transfer coefficient is a function of airspeed through the HX [45]. Thus, h is to be replaced with $h_{|u_i|}$, where $h_{|u_i|}$ is the average convective heat transfer coefficient at the airspeed of u_i . According to the air-side performance results of the plain fin and tube HX, the value of the heat transfer coefficient was calculated by [45,52]:

$$h_{|u_i|} = 900|u_i|^{0.71} \tag{8}$$

The HX thermal conductance curve shown in Fig. 9 was obtained using this equation. This empirical correlation was originally derived to be used at the rear door rack cooler [45]. Hence, it is also feasible for use with the perforated tiles. The properties and geometric characteristics of the plain fin and tube HX used in this study are provided in Table 2.

Where, D_i and D_o are the tube's inner and outer diameter. Next, F_{Th} is the fin thickness. Finally, F_p , P_{l_1} , and P_{l_t} are the fin pitch, longitudinal tube pitch, and transverse tube pitch, respectively. Since the embedded

floor HX airflow is passively driven, the cold airflow passing through the HX is highly affected by the pressure difference between the plenum and the CAC, and the HX geometrical properties. For these reasons, the CFD model was validated with the experimental measurements to ensures that the CFD is capable of predicting the pressure field accurately. Moreover, the HX geometrical parameters were obtained from previously introduced experimental work [52] (which was also used to model HX in the data center environment in previous work [45]). All these geometrical parameters were fed into the CFD model to accurately calculate the airflow through it by taking into account the flow resistance introduced by the HX, and the actual pressure difference between the plenum and the CAC. Considering that the row and rack manifolds are typically well-insulated, they were assumed to have adiabatic outer walls.

Even though row and rack manifolds are typically well insulated and negligible amount of heat is transferred through their walls introducing detailed energy and exergy analyses of the row manifold, and rack manifold would be an interesting topic to be investigated. However, considering the focus of the study, relying only on the CFD model is completely sufficient. The adopted detailed and validated CFD model was developed under the supervision of the CFD software company to ensure its reliability and accuracy. The CFD model was developed in the ES2 center for research purposes, and it has been tested by many researchers on many occasions against the experimental results. In each time, the model showed a great capability in predicting the actual performance in the data center. Moreover, CFD capabilities and reliability in modeling different components in data centers were assured in many studies. Considering the objectives of the study, we believe that our CFD model can accurately predict the performance of the overall system with an extremely high level of accuracy, especially that all components and geometrical parameters were fed into the model.

The preceding equations were used to model the embedded floor HX heat transfer characteristics, while the HX effectiveness was adapted to evaluate its thermal performance. The HX effectiveness is the actual heat transfer over the maximum possible heat transfer. In other words, the HX effectiveness can be defined as the actual heat transfer over the heat

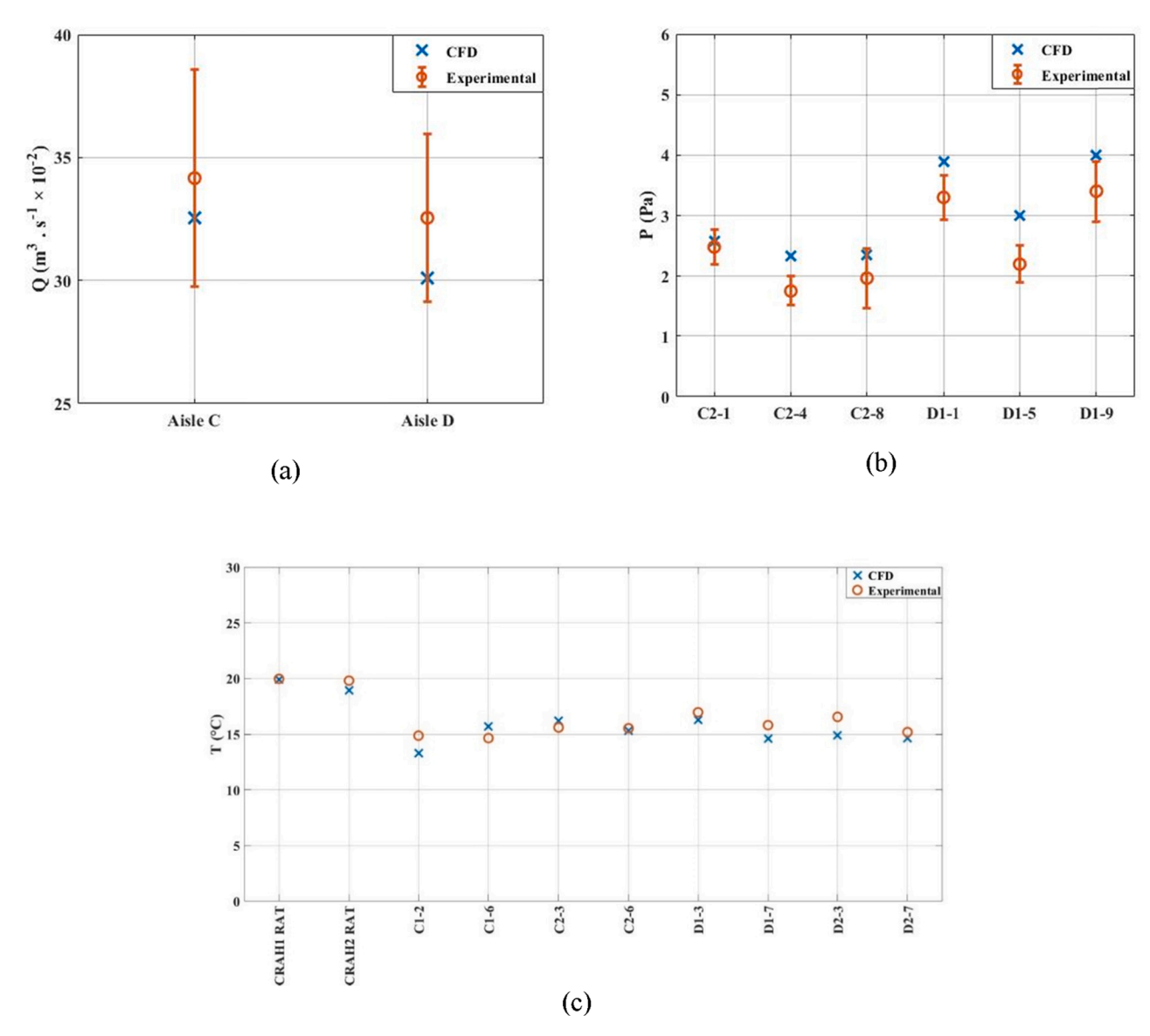


Fig. 8. Comparing of numerical model results with the experimental ones (a) average tile delivery (b) pressure (c) temperature.

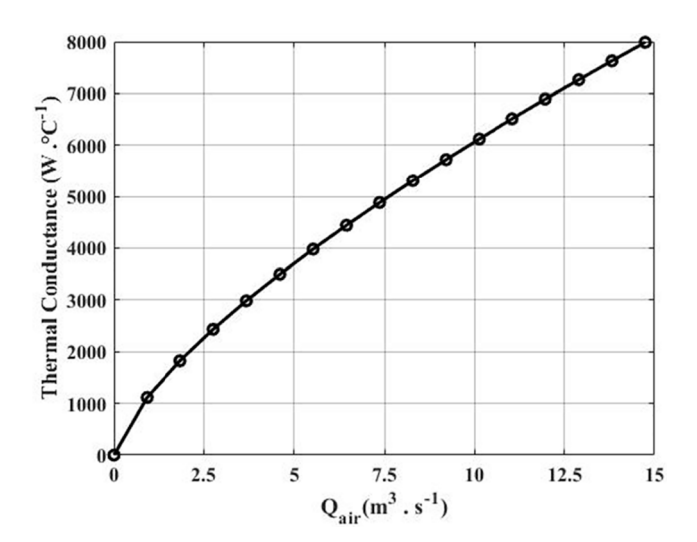


Fig. 9. HX thermal conductance curve.

transfer that could occur if the fluid temperature dropped down to the cold air inlet temperature. The HX effectiveness can be calculated using the following correlation:

$$Effectiveness = \frac{\dot{m}_{h}c_{p,h}(T_{h1} - T_{h2})}{(\dot{m}c_{p})_{min}(T_{h1} - T_{c1})} = \frac{\dot{m}_{c}c_{p,c}(T_{c2} - T_{c1})}{(\dot{m}c_{p})_{min}(T_{h1} - T_{c1})} \tag{9}$$

Where the rate of heat transferred from the coolant to the air is calculated by:

$$\dot{q} = h_{|u_i|} A(T_{h1} - T_{h2}) \tag{10}$$

3. Results and discussion

3.1. Design limitation (Heat exchanger cooling capacity)

After validating the numerical method and CFD model, the investigation was extended to include two modifications. First, the floor tiles in C and D were substituted with HXs of an equivalent open area, as shown in Fig. 10. Second, all racks in aisles C and D were homogenously repopulated with hybrid cooled (i.e. liquid and air) ITE. Each aisle HX was responsible for delivering the coolant to the corresponding aisle's ITE.

Table 2 Properties and geometric parameters of plain fin HX [52].

Property	Material	$D_i~(\textit{m}\times 10^{-3})$	$D_{o}~(\textit{m}\times 10^{-3})$	$F_{Th}~(\textit{m}\times 10^{-3})$	$F_p~(\textit{m}\times 10^{-3})$	$\text{Pi}_{\text{l}}~(\textit{m}\times 10^{-3})$	$\text{Pi}_{\text{t}}~(\textit{m}\times 10^{-3})$
Value	Copper	16	18	0.3	3.1	42	34

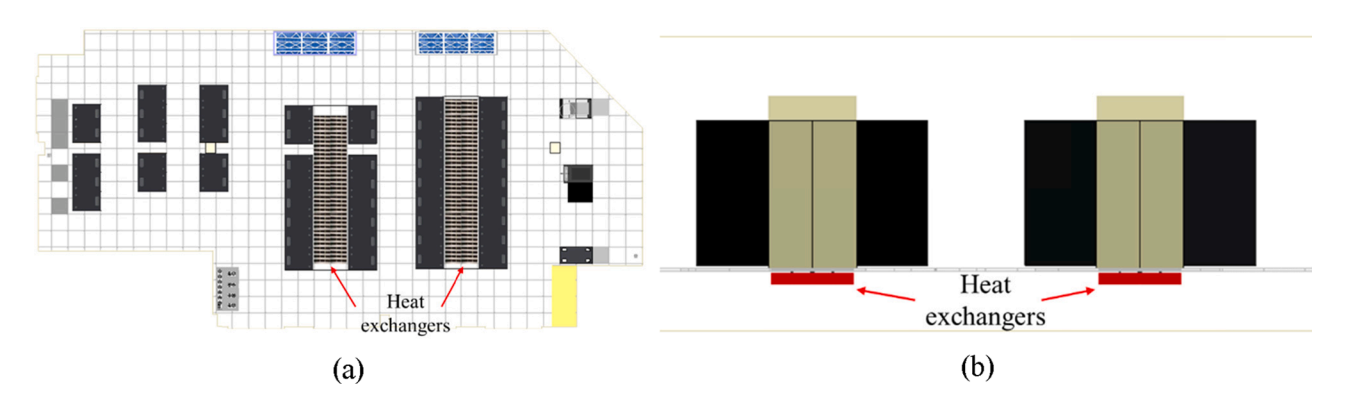


Fig. 10. Implementing HXs in the cold aisle floor (a) top view (b) front view.

To imitate a real-world scenario at the design point, the DC was set to operate within the typical operating conditions established by literature and in accordance with the ASHRAE guidelines [53,54]. In enumerating the advantages of the integrated floor HX, the CRAH units supply air temperature was set to 10 $^{\circ}\text{C}$, which can be easily achieved in the ES2 DC, and the CRAH units are adjusted to operate at full speed.

It was assumed that each ITE within racks in aisles C and D would dissipate 1 kW of heat. Only 70% of the heat dissipated was transferred to the coolant, while the rest was transferred to the air. Deionized water was selected as the coolant because of its superior thermophysical properties and high boiling point, the latter of which would prevent a phase change [55]. The coolant flowrate supplied to each rack was 18.93 LPM (5 GPM). A summary of the operating conditions is provided in Table 3.

Due to the fact that the HXs were embedded in the floor tiles, no physical elements of the DC were obstructed. Accordingly, no geometrical limitations were recognized. Consequently, it was expected that the predominant conceptual limitations of this system would be operationsbased. To be properly implemented, the operating conditions of this system needed to satisfy the limitations of the ITE Processor Junction Temperature (PJT), water flowrate per rack, Supply Water Temperature (SWT) to ITE, hot aisle (CRAH or CRAC) Return Air Temperature (RAT), and cold aisle (CRAH or CRAC) Supply Air temperature (SAT). The latter is substituted with the air temperature that leaves the embedded floor HX on account of the air temperature rise across the HX. A range of typical operating conditions and temperature limits are specified in Table 4. While Table 5 shows the thermophysical properties of the coolants. With regard to the pressure differential between the plenum and the cold aisle, there is no well-defined range. However, the literature showed that it could vary between 2.5 Pa and 25 Pa [56].

Table 3 DC operating conditions at design point.

Operating condition	Value
SAT of CRAH 1 (°C)	10.0
The rotational speed CRAH 1 fans	100%
SAT of CRAH 2 (°C)	10
The rotational speed CRAH 2 fans	100%
ITE power (kW)	1
Percent heat transferred to the coolant	70%
Coolant flowrate per rack $(m^3.s^{-1})$	$3.2 \times 10^{-4} \text{ (18.93 LPM)}$
Aisle C HX total coolant flowrate $(m^3.s^{-1})$	$50.5 \times 10^{-4} \text{ (302.8 LPM)}$
Aisle D HX total coolant flowrate $(m^3.s^{-1})$	$56.8 \times 10^{-4} (340.7 \text{ LPM})$

Table 4Summary of "typical" DC operating and temperature limits. [53,54]

Property	Value
Cold aisle SAT (°C)	10-32
Hot aisle RAT (°C)	15-60
Water supply temperature (°C)	20-60
Water flowrate per rack $(m^3.s^{-1})$	$(3.2-6.3) \times 10^{-4}$
PJT (°C)	85

Table 5Thermo-Physical properties of the used heat transfer fluids [57].

Property	Air	Deionized water
Density (kg.m ⁻³)	1.20	994.1
Specific Heat (J. Kg ⁻¹ °C ⁻¹)	1004	4180
Thermal Conductivity (W. m ⁻¹ °C ⁻¹)	0.026	0.613
Dynamic Viscosity (Pa. s ⁻¹)	1.81×10^{-5}	1.14×10^{-3}
Volumetric Heat Capacity (kJ. M ⁻³ °C ⁻¹)	1.15	4153.35

To identify the most critical operational limitations on the embedded floor HX's cooling capacity, different ITE loads were examined at the design point. The racks of aisles C and D were evenly populated with hybrid cooled ITE. The total individual rack power varied from 5 to 15 kW. Hence, the total ITE load in both aisles varied from 170 to 508 kW. Table 6 provides the results of the analysis for each aisle. It was assumed that CRAH 1 was assigned to aisle C and CRAH 2 was assigned to aisle D.

The table shows that when the ITE thermal load was increased only the cold aisle SAT exceeded its operational limitation, while all other conditions remained well within theirs. The maximum values calculated for the hot aisle RAT and return water temperature (RWT) were close to two-thirds of the limit. That of the water temperature supplied to the ITE was slightly higher than half the limit. That of the processor temperature was 30 $^{\circ}\mathrm{C}$ lower than the limit.

Based on the above, the SAT proved to be the critical condition that limited the HX cooling capacity and by extension the number of ITE that could be installed in each aisle. In aisles C and D, the total maximum number of ITE that could be installed was 14 and 13 per rack, respectively. Even though the number of ITE installed in the racks was higher for aisle C, aisle D was able to handle a higher cooling load than aisle C while supplying air at a temperature lower than 32 °C. The maximum cooling capacity for the HXs of aisles C and D was calculated as 156.8 and 163.8 kW, respectively. This can be explained by the fact that the

Table 6 HX cooling capacity limitation.

	Load per rack (kW)	Total ITE load (kW)	Air flowrate $(m^3$. $s^{-1})$	Aisle SAT (°C)	CRAH RAT (°C)	SWT (°C)	RWT (°C)	PJT (°C)	HX cooling load (kW)
Aisle C	5	80	5.508	18.6	20.2	17.5	20.1	36.8	56
	6	96	5.609	20.1	21.8	18.7	21.9	38.4	67.2
	7	112	5.693	21.6	23.4	19.9	23.6	40	78.4
	8	128	5.76	23	24.9	21.1	25.4	41.5	89.6
	9	144	5.826	24.4	26.5	22.3	27.1	43.1	100.8
	10	160	5.864	25.9	28.2	23.5	28.8	44.6	112
	11	176	5.909	27.4	29.9	24.7	30.6	46.2	123.2
	12	192	5.942	28.8	31.5	25.9	32.3	47.7	134.4
	13	208	5.991	30.2	33.2	27	33.9	49.5	145.6
	14	224	6.022	31.6	34.9	28.2	35.6	50.7	156.8
	15	240	6.051	33	36.7	29.3	37.3	52.1	168
Aisle D	5	90	6.042	18.7	19.1	18	20.7	37.4	63
	6	108	6.096	20.4	20.7	19.5	22.7	39.3	75.6
	7	126	6.177	21.9	22.4	20.9	24.6	41	88.2
	8	144	6.251	23.5	24.1	22.3	26.6	42.8	100.8
	9	162	6.322	25	25.7	23.7	28.5	44.5	113.4
	10	180	6.373	26.5	27.3	25.1	30.4	46.2	126
	11	198	6.41	28.1	28.8	26.5	32.3	47.9	138.6
	12	216	6.424	29.7	30.4	27.9	34.3	49.4	151.2
	13	234	6.479	31.1	32	29.2	36.1	51.2	163.8
	14	252	6.512	32.6	33.5	30.6	38	52.8	176.4
	15	270	6.543	34.1	34.9	32	39.9	54.4	189

HX in aisle D was bigger than that in aisle C, which means that more air was drawn through the HX.

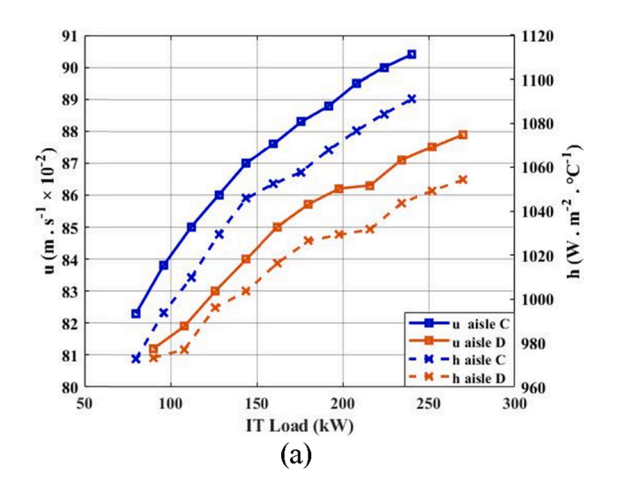
In addition, Table 6 shows that the air flowrate delivered to aisles C and D was dependent on the ITE load in these aisles. This is attributed to the variation in the pressure differential between the CAC and the underfloor plenum. The driving force of air movement across the heat exchanger is the pressure differential between the underfloor plenum and the CAC, which is affected by several factors such as plenum geometry, tiles perforation, CRAHs nominal supply, CRAHs location, ITE load, and ITE cooling demand [58,59]. When more ITE was installed, more air was driven from the CAC to the hot aisle by their fans. Accordingly, the pressure inside the CAC decreased and the pressure differential between the underfloor plenum and the CAC expanded, which means additional air was delivered to the cold aisle from the underfloor plenum. It is worth mentioning that for all discussed cases in this work, the pressure differential across the HXs was observed to lie within the ranges reported by literature [56]. Fig. 11 depicts the impact of the ITE load on the air velocity in the HX, the HX heat transfer coefficient, and the HX effectiveness for both aisles.

It can be noted from Fig. 11 that both the velocity and the heat transfer coefficient of air passing through the HX rose with the ITE load increment. Moreover, the air velocity in aisle C's HX was found to be

higher than that in aisle D which resulted in a higher heat transfer coefficient in aisle C's HX. Thereby, the HX in aisle C was found to have a higher effectiveness than that in aisle D. Fig. 11 also shows that the HX's effectiveness slightly decreased with an increase in the ITE load This was because the amount of heat being transferred to the water from the ITE increased, therefore the temperature gradient between the inlet water and the outlet air also increased. However, this effect was considered minimal, seeing as the water velocity remained constant and the air velocity only varied slightly.

3.2. Operational conditions parametric study

To quantify the effects of the operational conditions on the HX's performance, 36 CFD models were solved considering various DC operational conditions. The CRAH unit was set to supply air at four different temperatures (10 °C, 15 °C, 20 °C, and 25 °C) with three different water flowrate deliveries per rack (3.2 $\times 10^{-4} m^3.s^{-1}$, 4.7 $\times 10^{-4} m^3.s^{-1}$, 6.3 $\times 10^{-4} m^3.s^{-1}$). These operational conditions were investigated considering ITE with various hybridization ratios (60%, 70%, 80%), in other words, the percent of heat transferred to water (60%, 70%, and 80%). Table 7 describes the operational conditions for all those cases. It is worth mentioning that the hybridization ratio is not



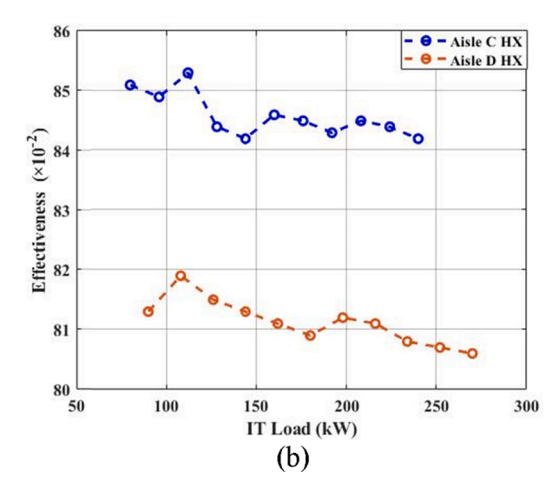


Fig. 11. Impact of ITE load on the (a) air velocity, heat transfer coefficient, and (b) the effectiveness of the HX.

Table 7Considered cases details.

Cases	CRAH SAT (°C)	Percent liquid cooled (%)	Rack Water flowrate $(m^3.s^{-1})$
1,2,3,	10	60	$(3.2, 4.7, 6.3) \times 10^{-4}$
4,5,6	10	70	$(3.2, 4.7, 6.3) \times 10^{-4}$
7,8,9	10	80	$(3.2, 4.7, 6.3) \times 10^{-4}$
10,11,12	15	60	$(3.2, 4.7, 6.3) \times 10^{-4}$
13,14,15	15	70	$(3.2, 4.7, 6.3) \times 10^{-4}$
16,17,18	15	80	$(3.2, 4.7, 6.3) \times 10^{-4}$
19,20,21	20	60	$(3.2, 4.7, 6.3) \times 10^{-4}$
22,23,24	20	70	$(3.2, 4.7, 6.3) \times 10^{-4}$
25,26,27	20	80	$(3.2, 4.7, 6.3) \times 10^{-4}$
28,29,30	25	60	$(3.2, 4.7, 6.3) \times 10^{-4}$
31,32,33	25	70	$(3.2, 4.7, 6.3) \times 10^{-4}$
34,35,36	25	80	$(3.2, 4.7, 6.3) \times 10^{-4}$

being adjusted or controlled, actually it is a property of the ITE equipment, depending on the amount of heat dissipated by its various components. Where the components that has cold plates will dissipate most of its heat into the liquid, while other components will dissipate its heat to the air. Thus, different ITE will exhibit different percent of hybridization. Moreover, hybridization ratio depends on the used liquid cooling solution efficiency and its capability for picking heat from the components. Hence the cold plate design, size, thermal interface material, and coolant thermo-physical properties are all affecting the hybridization ratio. The reason behind investigating different percent of hybridization is to reveal how installing different ITE with different hybridization ratios will affect the HXs performance.

Both CRAH units were powered at full cooling capacity. In addition, ITE dissipated power and all other variables of the DC remained unchanged. Thereafter, the HXs performance was assessed based on the cooling capacity and effectiveness. The HX cooling capacity and the total ITE heat load were determined based on maximum values that satisfied the operating condition requirements. Moreover, the Power Usage Effectiveness (PUE) was introduced to evaluate how the DC performed in terms of energy efficiency under the different operating conditions while the HX's were installed [60]. The PUE was calculated using the following equations [61]:

$$PUE = \frac{Total\ facility\ power}{ITE\ power}$$
 (11)

Total facility power=ITE power+PDU loss+UPS loss+lighting power +cooling unit input power+chilled water system power +miscellaneous power system loss (12)

where ITE power represents the actual power used by the ITE, PDU loss represents the total power lost from all PDU within the DC, UPS loss represents the total power lost through the UPS, lighting power represents the total light load, and cooling unit input power represents the units' fan powers. Table 8 summarizes their individual contribution to the total facility power in this study.

The data presented in Table 8 was calculated using the number of units, the heat dissipation property tables, and power consumption rates

Table 8Summary of individual components contribution to facility total power.

Component	Power (kW)
PDU loss	1.10
UPS	15.30
Lighting	3.60

provided by the vendors. While for the CRAH unit, the code calculates its power consumption at different operating conditions using the vendor's

technical manual and the fan affinity law $\frac{p_1}{P_2} = \left(\frac{N_1}{N_2}\right)^3$. The chilled water

system power was either defined as a fixed value or as a function of the chilled water temperature. However, this was disregarded from the author's calculations. The reason being that the ES2 DC has no specified chiller because it receives its chilled water from the main campus chiller. An ideal PUE is 1.0, which indicates that there is no power lost through other components in the DC, and higher PUE values indicate higher power losses in the system [62]. Table 9 introduces a summary of the parametric study results. The results presented in this Table shows a potential optimization study using the NSGA-II algorithm, similar to what has been done in [63].

Considering the parameters shown in Table 9, note that the air temperature supplied to the HX had a crucial impact on the HX's cooling capacity in aisle C, the maximum HX cooling capacity of 156.8 kW was achieved when the air supplied by the CRAH unit was at 10 $^{\circ}$ C and when 70% of the ITE dissipated heat was transferred to the water. Meanwhile, the maximum HX cooling capacity in aisle D was achieved when the CRAH unit SAT was 10 $^{\circ}$ C and when the percent of heat transferred to the liquid was 80%. When the CRAH unit SAT increased to 25 $^{\circ}$ C, the HX cooling capacity dropped to 44.8 kW and 43.2 kW in aisles C and D, respectively. Consequently, the PUE rose significantly with increases in the SAT.

The influence of the hybridization percent on the cooling capacity was minimal. However, it was greatly correlated to the number of ITE that the HX could support. Consider that when less heat is picked up by the water it also follows that less heat is transferred to the HX. Therefore, the PUE will decrease and the HX can support a larger number of ITE. On the other hand, less heat is transferred to the water means more heat must be transferred to the air. Fig. 12 demonstrates the impact of the hybridization percent on the CRAH units' RATs.

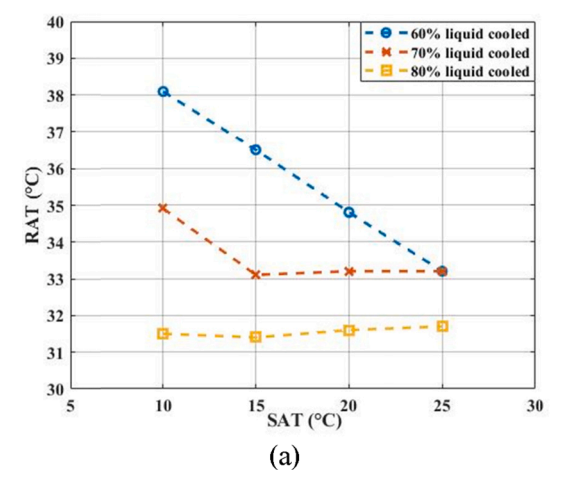
From Fig. 12 it can be inferred that the hybridization ratio had a considerable effect on the CRAH units' RATs, especially at lower SATs. Even if the CRAH units SAT is not directly correlated to the RAT (seeing that the air is preheated to almost 32 °C in HX before entering the cold aisle in all cases), SAT determines the number of ITE installed in the aisle. At lower SATs, more ITE can be installed. However, the number of ITE is more sensitive to variations in the hybridization ratio at lower SATs than at higher SATs. For instance, when the CRAH units' SATs were set to 10 °C and the heat transferred to the water was increased from 60% to 80%, the number of possible ITE decreased from 256 to 192. When the CRAH units' SATs were set to 25 °C and the heat transferred to the water was increased from 60% to 80%, the number of possible ITE only decreased from 64 to 48.

Moreover, the percent of heat dissipated to the liquid affected the rise in air temperature across the ITE, which in turn impacted the CRAH units' RATs. When the percent of heat picked up by water was increased from 60% to 80%, the amount of heat picked up by air decreased by 200 W. The average rise in air temperature across the ITE was 9.2 °C, 5.7 °C, and 3.8 °C for 60%, 70%, and 80% of heat transferred to water, respectively. The maximum air temperature is observed in the hot aisle just as the air is about to cool down before returning to the CRAH units, which is due to the mixing of the room air and the cold air from the other aisles. This justifies why Fig. 12 shows that the CRAH units' RATs are lower than the air temperature supplied to the cold aisle in some cases. To form a better understanding of the air temperature distribution within the DC, the air temperature distribution was plotted 1.9 m above the raised floor to match the height of the CRAH units, as shown in Fig. 13. These three temperature distributions represent the cases when the SAT was set to 10 $^{\circ}$ C and the percent of liquid-cooled ITE was and 60%, 70%, and 80%.

In view of the last parameter, increasing the water flowrate did not show any negative influence on the HX cooling capacity or the PUE. In

Table 9Operational parametric study.

Case	HX C cooling capacity (kW)	HX C effectivness	HX D cooling capacity (kW)	HX D effectivness	PUE	Case	HX C cooling capacity (kW)	HX C effectivness	HX D cooling capacity (kW)	HX D effectivness	PUE
1	153.6	0.84	162	0.81	1.08	19	76.8	0.83	86.4	0.82	1.15
2	153.6	0.89	162	0.84	1.08	20	76.8	0.88	86.4	0.86	1.15
3	153.6	0.91	162	0.87	1.08	21	76.8	0.9	86.4	0.87	1.15
4	156.8	0.84	163.8	0.81	1.09	22	78.4	0.86	88.2	0.82	1.17
5	156.8	0.89	163.8	0.85	1.09	23	78.4	0.88	88.2	0.85	1.17
6	156.8	0.91	163.8	0.87	1.09	24	78.4	0.91	88.2	0.82	1.17
7	153.6	0.84	172.8	0.81	1.1	25	76.8	0.84	86.4	0.82	1.2
8	153.6	0.89	172.8	0.85	1.1	26	76.8	0.88	86.4	0.85	1.2
9	153.6	0.91	172.8	0.87	1.1	27	76.8	0.9	86.4	0.87	1.2
10	115.2	0.84	118.8	0.81	1.1	28	38.4	0.83	43.2	0.82	1.3
11	115.2	0.88	118.8	0.85	1.1	29	38.4	0.86	43.2	0.88	1.3
12	115.2	0.91	118.8	0.87	1.1	30	38.4	0.89	43.2	0.87	1.3
13	112	0.84	126	0.81	1.12	31	44.8	0.83	37.8	0.83	1.34
14	112	0.89	126	0.85	1.12	32	44.8	0.87	37.8	0.86	1.34
15	112	0.91	126	0.87	1.12	33	44.8	0.9	37.8	0.89	1.34
16	115.2	0.84	129.6	0.81	1.13	34	38.4	0.84	43.2	0.82	1.4
17	115.2	0.89	129.6	0.85	1.13	35	38.4	0.87	43.2	0.86	1.4
18	115.2	0.91	129.6	0.88	1.13	36	38.4	0.9	43.2	0.88	1.4



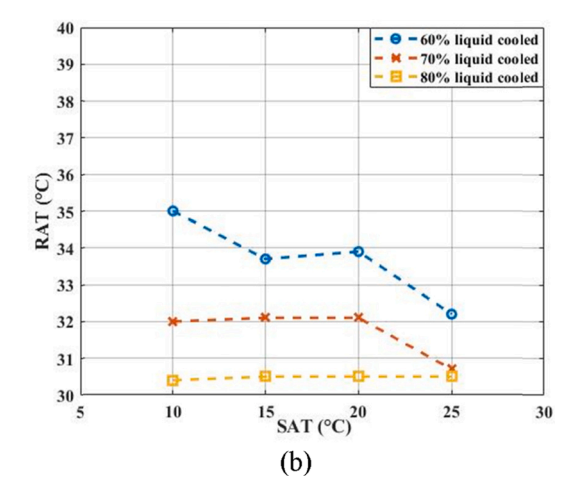


Fig. 12. IT load impact on (a) CRAH 1 (b) CRAH 2 return air temperature.

fact, it was shown to improve the HX's effectiveness. [Furthermore, increases in the water flowrate were reflected in the water temperatures supplied to the ITE, and consequently, the processor junction temperatures. Fig. 14 illustrates the impact of the water flowrate on the SWT, the processor temperature, and the RWT.

Based on Fig. 14, increasing the water flowrate with a constant SAT and hybridization ratio generally increased the SWT. This occurred because increasing the water velocity meant that less time was available for the water to dissipate heat to the air via the HX, hence the temperature gradient between the outlet water and the outlet air increased. Furthermore, the SAT was shown to have a direct relationship with the SWT, while the percent heat transferred to the water was found to have an inverse relationship with the SWT. By investigating these correlations, it turns that the IT load variation and the temperature gradient between SAT and the SWT that occurs due to changing the SAT and the hybridization ratio are the reasons behind developing such correlations.

Delivering more water to the ITE improved the heat transfer coefficient and decreased the temperature gradient between the water and the ITE processor even if the SWT temperature was higher. However, this improvement had a limit wherein introducing more water resulted in no difference to the heat transferred to the ITE. This illustrates why Fig. 14 shows that the PJT was more sensitive to the water flowrate at lower SATs. At low SATs, less water was available to each individual ITE because it was distributed across a larger number of ITE. At high SATs, more water was available to each individual ITE because it was

distributed across a smaller number of ITE. Therefore, when the flowrate was increased at an SAT of 25 $^{\circ}$ C, the change in PJT was negligible. This also applied to the RWT, which appeared to be more affected by changes in the water flow rate at low SATs.

When the flowrate was doubled at an SAT of 10 $^{\circ}$ C, the change in PJT was still considered negligible, decreasing by about 1 $^{\circ}$ C. Even so, this result cannot be generalized for ITE with other types of internal cooling loops. It is possible that other ITE could exhibit significant changes in processor temperatures when the water flowrate is altered. Some powerful ITE has a required minimum for water flowrate delivery. Based on this, the water flowrate is a critical factor for the cooling loops, but not for the HX if enough water is supplied.

3.3. Alternative implementation

With the goal of overcoming the operational constraints imposed by the cold aisle SAT, an alternative HX configuration was examined. The alternative configuration is illustrated in Fig. 15. Therein, aisle D's HX was relocated to the hot aisle between aisles C and D, while perforated tiles were installed in both aisles with a staggered formation. The floor tile open area ratio was adapted to assure that the aisles were provisioned with adequate cold air by maintaining positive pressure. In this study, the CFD results showed that a floor tile open area ratio of 19% could sufficiently provision the aisle for different IT loads. In consonance with the literature, the amount of airflow rate demand per 1 kW of heat

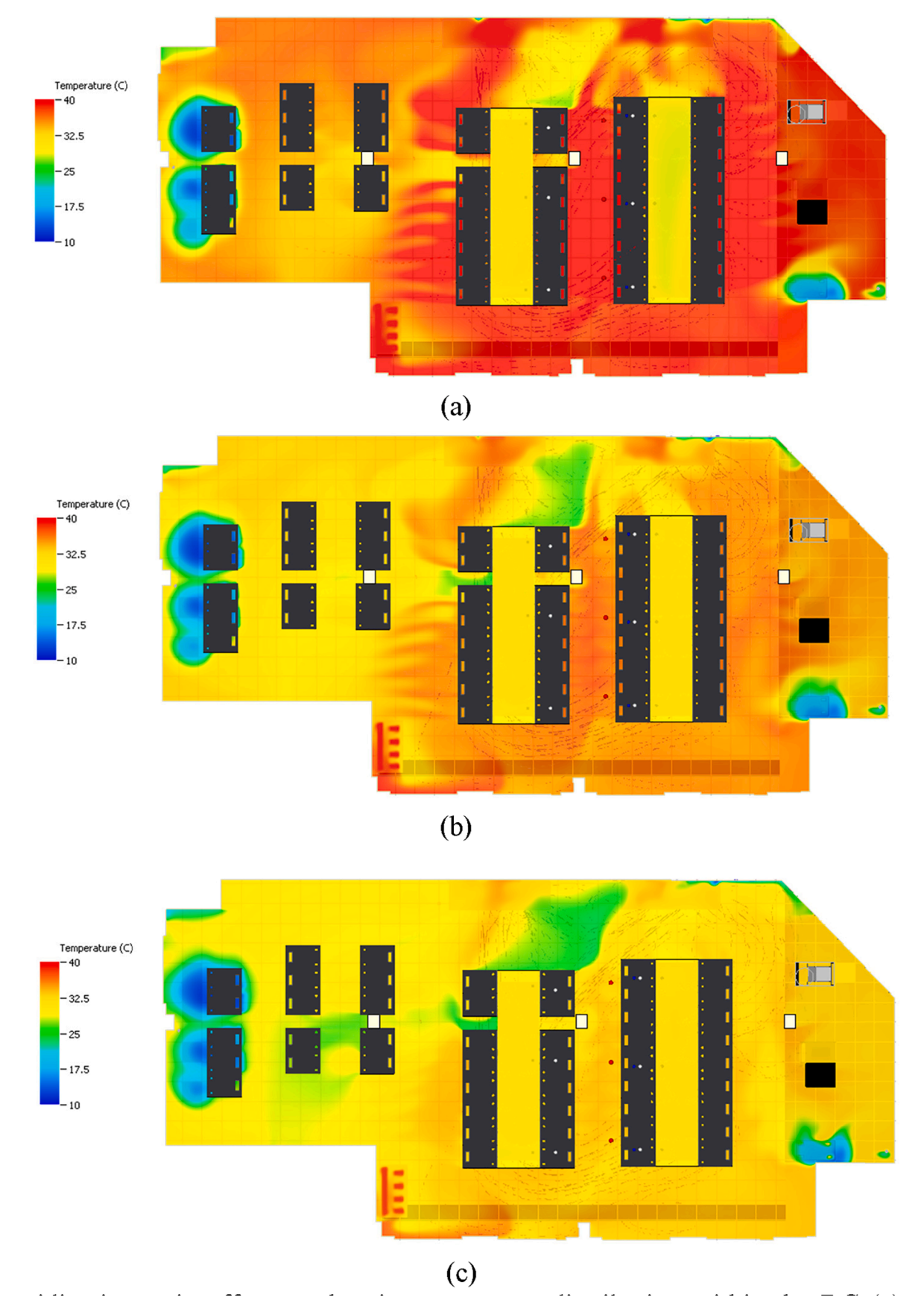


Fig. 13. Hybridization ratio effect on the air temperature distribution within the DC (a) 60% liquid-cooled (b) 70% liquid-cooled (c) 80% liquid-cooled.

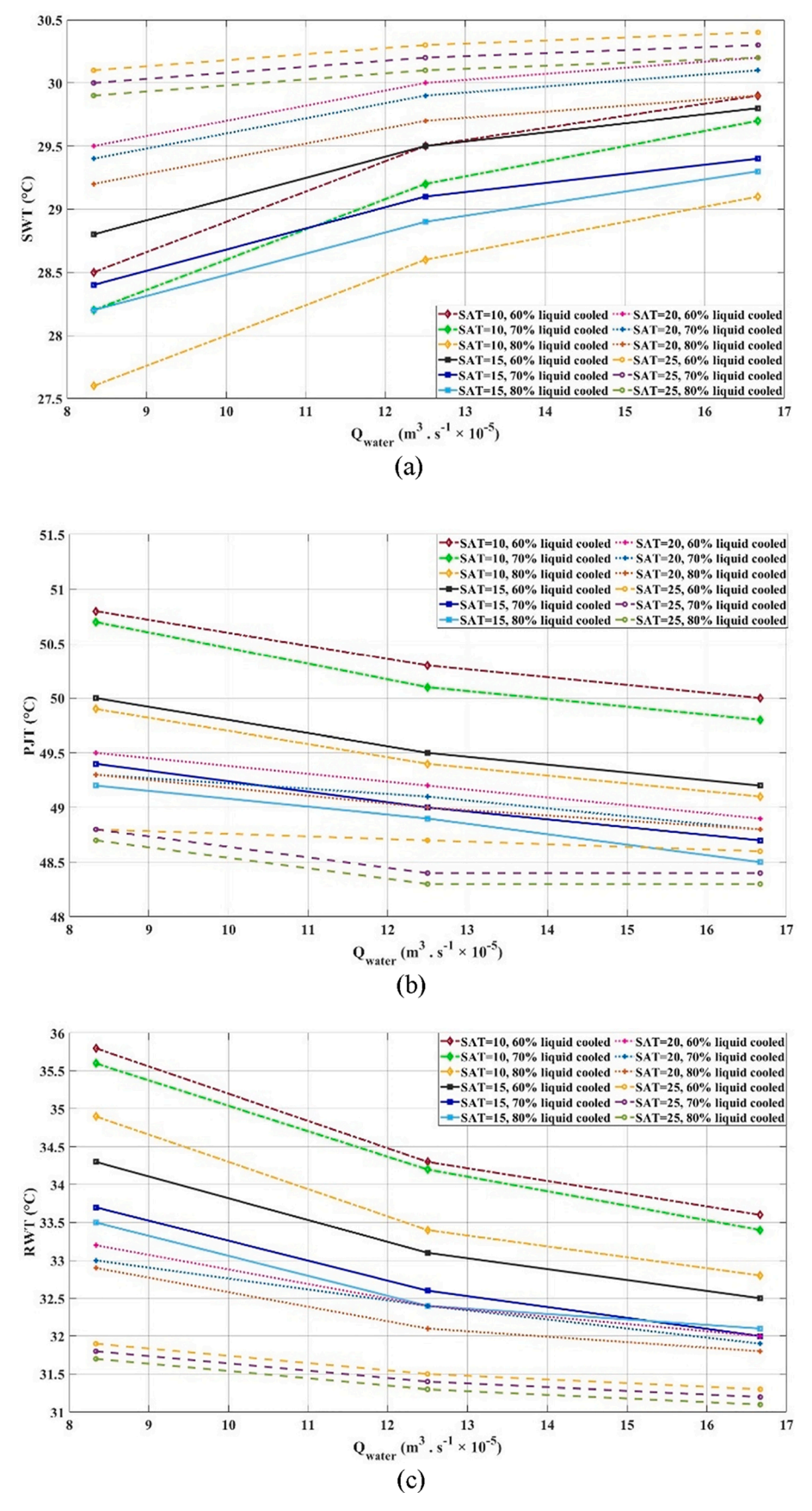


Fig. 14. Water flowrate impact on (a) SWT (b) PJT (c) RWT.

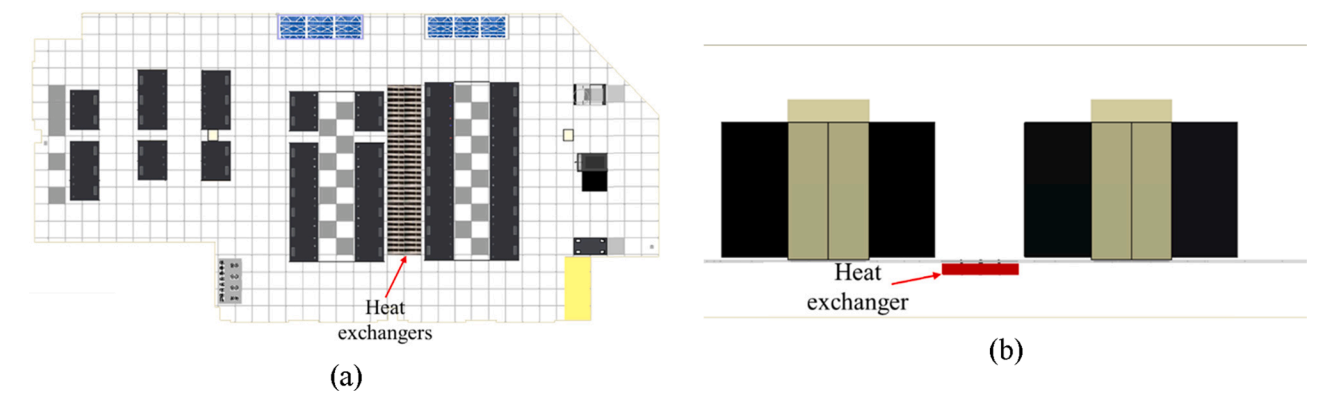


Fig. 15. Second configuration was made by installing one HX in the hot aisle (a) top view (b) front view.

dissipation by the IT was calculated to be around $4.72 \times 10^{-2} \ m^3$. s^{-1} (100 cubic feet per minute) [64,65].

In this configuration, heat from the hot water returning from the racks was ejected into the hot aisle via the HX, which was set up to supply water to racks in both aisles C and D. Unlike in the cold aisle configuration, in this hot aisle configuration the HX's capacity was not restricted by the SAT. Instead, here the HX turned out to be limited by the RAT, whilst all other operating conditions ran within their typical ranges. Table 10 shows the maximum heat capacity of the HX that satisfies all the typical DC operational and temperature limits. In line with the previous section, the HX capacity was specified at various SATs with racks that were populated with 70% liquid-cooled ITE.

As demonstrated by the results in Table 10, in this configuration the HX showed better cooling capacity than in the previous configuration. This can be attributed to the increase in the airflow rate through the HX as well as the increase in the temperature gradient across it. For the cold aisle configuration, the HX's cooling capacity decreased when the SAT increased, but in the hot aisle configuration, that trend was not the same. In the hot aisle configuration, even with the highest SAT, the cooling capacity was calculated to be 309 kW, which is higher than the maximum HX cooling capacity achieved by either of the HXs installed in the cold aisle configuration. Therefore, this configuration is preferable to the previous one especially in DCs that may be struggling to reach a low SAT. With respect to overall DC efficiency, for the hot aisle configuration, the PUE results showed that the DC operated more efficiently and that its efficiency was less affected by variations in the SAT.

Accordingly, it is recommended that a careful analysis of this HX configuration is performed before installation to estimate the HX's cooling capacity and obtain the best performance possible. The merit of this configuration is that it can be easily resized to support the required cooling load, so long as adequate air is provided. Hence, it can be made one or two tiles small to support just one ITE rack or it can be made larger to support a whole aisle of ITE racks.

4. Conclusions

Relying solely on air to cool ITE in DCs has become increasingly difficult due to the continuous increase of ITE powder densities. In this study, a potential solution to facilitate the deployment of liquid cooling when a chilled water source is not accessible in a DC was introduced. First, a configuration with the HXs embedded in the floor tiles of both cold aisles was studied. The results showed that the HXs' maximum cooling capacities equaled 163.8 kW and 156.8 kW for aisles C and D, respectively. The cooling capacity here was constrained by the typical DC operational and temperature limits.

Thereafter, an operational parametric study was carried out to inspect the impact of the SAT, percent heat dissipated to liquid coolant, and liquid flow rate on the HX's performance. It was found that increasing the SAT caused a sharp decline in the HX's cooling capacity,

Table 10
HX performance under different SATs.

CRAH SAT (°C)	Load per rack (kW)	Air flowrate $(m^3. s^{-1})$	RAT (°C)	SWT (°C)	HX cooling capacity (kW)	PUE
10 15 20	21 19 16	8.498 8.726 8.479	59.1 58.1 57.5	52.1 51.1 52.6	499.8 452.2 380.8	1.06 1.06 1.07
25	13	8.552	57.7	53.4	309.4	1.09

while changing other parameters had minimal impact. On the other hand, it was found that increasing the water flowrate improved the HX's effectiveness.

Lastly, an alternative configuration with one HX embedded in the floor tile of the hot aisle between aisles C and D was studied. This configuration showed better performance in terms of the HX's cooling capacity. Additionally, in this arrangement, the HX proved to be less sensitive to the CRAH units' SATs. Herein, the highest cooling capacity of 499.8 kW was achieved when the SAT was 10 $^{\circ}$ C, which was accompanied by a DC PUE of 1.06.

For a future work, many research interesting investigations could be conducted such as analyzing the heat exchanger, row manifold, and rack manifold in terms of both energy and exergy. Also, a geometrical optimization study could be performed on the heat exchanger design.

CRediT authorship contribution statement

Yaman M. Manaserh: Conceptualization, Methodology, Data curation, Formal analysis, Investigation, Resources, Software, Supervision, Validation, Visualization, Writing – original draft, Writing – review & editing. Mohammad I. Tradat: Investigation, Resources, Software, Supervision, Validation, Visualization, Writing – review & editing. Ahmad R. Gharaibeh: Investigation, Resources, Software, Supervision, Validation, Visualization, Writing – review & editing. Bahgat G. Sammakia: Supervision, Project administration, Writing – review & editing. Russ Tipton: Supervision, Writing – review & editing.

Declaration of Competing Interest

The authors declare that they have no known competing financial interests or personal relationships that could have appeared to influence the work reported in this paper.

Acknowledgments

We would like to acknowledge Future Facilities Ltd. We would also like to thank the ES2 Partner Universities for their support and advice. This work is supported by NSF IUCRC Award No. IIP- 1738793 and MRI

Award No. CNS1040666.

Appendix A. Operating saving opportunities in the fan pumping power

Number of units	Annual energy consumption (Mwh)	Annual operating cost (\$)
1	26.3	3469
10	262.8	34,663
20	525.6	69,327
30	788.4	103,990
40	1051.2	138,653
50	1314	173,317

References

- [1] Al-Ghussain L, Abubaker AM, Ahmad AD. Superposition of renewable-energy supply from multiple sites maximizes demand-matching: Towards 100% renewable grids in 2050. Appl Energy 2021;284:116402.
- [2] Ahmad AD, Abubaker AM, Najjar YS, Manaserh YMA. Power boosting of a combined cycle power plant in Jordan: An integration of hybrid inlet cooling & solar systems. Energy Convers Manage 2020;214:112894.
- [3] Manaserh YMA, Abubaker AM, Ahmad AD, Ata AB, Najjar YS, Akafuah NK. Assessment of integrating hybrid solar-combined cycle with thermal energy storage for shaving summer peak load and improving sustainability. Sustainable Energy Technol Assess 2021;47:101505.
- [4] Glanz J. Power, pollution and the internet. NY Times 2012.
- [5] Koomey JG. Growing in data center electricity use 2005 to 2010. 2011.
- [6] Chen M, Gao C, Song M, Chen S, Li D, Liu Q. Internet data centers participating in demand response: A comprehensive review. Renew Sustain Energy Rev 2020;117: 109466. https://doi.org/10.1016/j.rser.2019.109466.
- [7] Kwon S. Ensuring renewable energy utilization with quality of service guarantee for energy-efficient data center operations. Appl Energy 2020;276:115424. https://doi.org/10.1016/j.apenergy.2020.115424.
- [8] Chu W-X, Hsu C-S, Tsui Y-Y, Wang C-C. Experimental investigation on thermal management for small container data center. Journal of Building Engineering. 2019;21:317–27.
- [9] Shuja J, Gani A, Shamshirband S, Ahmad RW, Bilal K. Sustainable cloud data centers: a survey of enabling techniques and technologies. Renew Sustain Energy Rev 2016;62:195–214.
- [10] Wang X, Li H, Wang Y, Zhao J, Zhu J, Zhong S, et al. Energy, exergy, and economic analysis of a data center energy system driven by the CO2 ground source heat pump: Prosumer perspective. Energy Convers Manage 2021;232:113877. https:// doi.org/10.1016/j.enconman.2021.113877.
- [11] Ma Y, Ma G, Zhang S, Xu S. Experimental investigation on a novel integrated system of vapor compression and pump-driven two phase loop for energy saving in data centers cooling. Energy Convers Manage 2015;106:194–200.
- [12] Tradat MI, Sammakia BG, Hoang CH, Alissa HA. An experimental and numerical investigation of novel solution for energy management enhancement in data centers using underfloor plenum porous obstructions. Appl Energy 2021;289: 116663.
- [13] Ni J, Bai X. A review of air conditioning energy performance in data centers. Renew Sustain Energy Rev 2017;67:625–40.
- [14] Saber HH, AlShehri SA, Maref W. Performance optimization of cascaded and noncascaded thermoelectric devices for cooling computer chips. Energy Convers Manage 2019;191:174–92.
- [15] Kanargi B, Lee PS, Yap C. A numerical and experimental investigation of heat transfer and fluid flow characteristics of an air-cooled oblique-finned heat sink. Int J Heat Mass Transf 2018;116:393–416.
- [16] Zhou W, Li Y, Chen Z, Deng L, Gan Y. A novel ultra-thin flattened heat pipe with biporous spiral woven mesh wick for cooling electronic devices. Energy Convers Manage 2019;180:769–83.
- [17] Gilmore N, Timchenko V, Menictas C. Open manifold microchannel heat sink for high heat flux electronic cooling with a reduced pressure drop. Int J Heat Mass Transf 2020;163:120395.
- [18] Pan Q, Peng J, Wang R. Application analysis of adsorption refrigeration system for solar and data center waste heat utilization. Energy Convers Manage 2021;228: 113564.
- [19] Fakhim B, Behnia M, Armfield SW, Srinarayana N. Cooling solutions in an operational data centre: A case study. Appl Therm Eng 2011;31(14-15):2279–91.
- [20] Cho J, Kim Y. Improving energy efficiency of dedicated cooling system and its contribution towards meeting an energy-optimized data center. Appl Energy 2016; 165:967–82.
- [21] Chen H, Peng Y-H, Wang Y-L. Thermodynamic analysis of hybrid cooling system integrated with waste heat reusing and peak load shifting for data center. Energy Convers Manage 2019;183:427–39.
- [22] Moazamigoodarzi H, Tsai PJ, Pal S, Ghosh S, Puri IK. Influence of cooling architecture on data center power consumption. Energy. 2019;183:525–35.

- [23] Tatchell-Evans M, Kapur N, Summers J, Thompson H, Oldham D. An experimental and theoretical investigation of the extent of bypass air within data centres employing aisle containment, and its impact on power consumption. Appl Energy 2017;186:457–69.
- [24] Chu W-X, Wang C-C. A review on airflow management in data centers. Appl Energy 2019;240;84–119.
- [25] Song Z, Murray BT, Sammakia B. Airflow and temperature distribution optimization in data centers using artificial neural networks. Int J Heat Mass Transf 2013;64:80–90.
- [26] Fulpagare Y, Mahamuni G, Bhargav A. Effect of plenum chamber obstructions on data center performance. Appl Therm Eng 2015;80:187–95.
- [27] Tuckerman DB, Pease RFW. High-performance heat sinking for VLSI. IEEE Electron Device Lett 1981;2:126–9.
- [28] Lee P-S, Garimella SV, Liu D. Investigation of heat transfer in rectangular microchannels. Int J Heat Mass Transf 2005;48(9):1688–704.
- [29] Kandlikar SG, Bapat AV. Evaluation of jet impingement, spray and microchannel chip cooling options for high heat flux removal. Heat Transfer Eng 2007;28: 911–23.
- [30] Zimmermann S, Meijer I, Tiwari MK, Paredes S, Michel B, Poulikakos D. Aquasar: A hot water cooled data center with direct energy reuse. Energy. 2012;43:237–45.
- [31] Carbó A, Oró E, Salom J, Canuto M, Macías M, Guitart J. Experimental and numerical analysis for potential heat reuse in liquid cooled data centres. Energy Convers Manage 2016;112:135–45.
- [32] Gao T, David M, Geer J, Schmidt R, Sammakia B. Experimental and numerical dynamic investigation of an energy efficient liquid cooled chiller-less data center test facility. Energy Build 2015;91:83–96.
- [33] David MP, Iyengar M, Parida P, Simons R, Schultz M, Gaynes M. et al. Experimental characterization of an energy efficient chiller-less data center test facility with warm water cooled servers. 2012 28th Annual IEEE Semiconductor Thermal Measurement and Management Symposium (SEMI-THERM). IEEE2012. pp. 232-7.
- [34] Schmidt R, Steinke M, Shelnutt A. Moderating the impact of integrating watercooled servers into data centers. ASHRAE Journal. 2019;61.
- [35] M.C.F. Ashrae Technica lCommittee9.9, DataCenters, Technology Spaces and Electronic Equipment. Water-Cooled Servers Common Designs, Components, and Processes. Atlanta 2019.
- [36] Mohammed Adham A, Mohd-Ghazali N, Ahmad R. Thermal and hydrodynamic analysis of microchannel heat sinks: A review. Renew Sustain Energy Rev 2013;21: 614–22.
- [37] Naqiuddin NH, Saw LH, Yew MC, Yusof F, Ng TC, Yew MK. Overview of microchannel design for high heat flux application. Renew Sustain Energy Rev 2018;82: 001 14
- [38] Kempers R, Colenbrander J, Tan W, Chen R, Robinson A. Experimental characterization of a hybrid impinging microjet-microchannel heat sink fabricated using high-volume metal additive manufacturing. International Journal of Thermofluids. 2020;5:100029.
- [39] Birbarah P, Gebrael T, Foulkes T, Stillwell A, Moore A, Pilawa-Podgurski R, et al. Water immersion cooling of high power density electronics. Int J Heat Mass Transf 2020;147:118918.
- [40] Corp VG. Liquid to Air Heat Exchanger for. Chip Cooling. 2019.
- [41] Tradat MI, Alissa HA, Nemati K, Khalili S, Sammakia BG, Seymour MJ. et al. Impact of elevated temperature on data center operation based on internal and external IT instrumentation. 2017 33rd Thermal Measurement, Modeling & Management Symposium (SEMI-THERM). IEEE2017. pp. 108-14.
- [42] Manaserh YM, Tradat MI, Mohsenian G, Sammakia BG, Seymour MJ. General guidelines for commercialization a small-scale in-row cooled data center: a case study. 2020 36th Semiconductor Thermal Measurement, Modeling & Management Symposium (SEMI-THERM). IEEE2020. pp. 48-55.
- [43] Meng X, Zhou J, Zhang X, Luo Z, Gong H, Gan T. Optimization of the thermal environment of a small-scale data center in China. Energy. 2020;196:117080.
- [44] Athavale J, Yoda M, Joshi Y. Comparison of data driven modeling approaches for temperature prediction in data centers. Int J Heat Mass Transf 2019:135:1039–52.
- [45] Almoli A, Thompson A, Kapur N, Summers J, Thompson H, Hannah G. Computational fluid dynamic investigation of liquid rack cooling in data centres. Appl Energy 2012;89:150–5.

- [46] Silva-Llanca L, Ortega A, Fouladi K, del Valle M, Sundaralingam V. Determining wasted energy in the airside of a perimeter-cooled data center via direct computation of the Exergy Destruction. Appl Energy 2018;213:235–46.
- [47] Yuan X, Xu X, Wang Y, Liu J, Kosonen R, Cai H. Design and validation of an airflow management system in data center with tilted server placement. Appl Therm Eng 2020;164:114444.
- [48] Mahmoud H, Kriaa W, Mhiri H, Le Palec G, Bournot P. A numerical study of a turbulent axisymmetric jet emerging in a co-flowing stream. Energy Convers Manage 2010:51:2117–26.
- [49] Chattopadhyay H, Kundu A, Saha BK, Gangopadhyay T. Analysis of flow structure inside a spool type pressure regulating valve. Energy Convers Manage 2012;53: 196–204.
- [50] Xiang H, Wang Y, Zhu L, Han X, Sun Y, Zhao Z. 3D numerical simulation on heat transfer performance of a cylindrical liquid immersion solar receiver. Energy Convers Manage 2012;64:97–105.
- [51] Conner ME, Baglietto E, Elmahdi AM. CFD methodology and validation for singlephase flow in PWR fuel assemblies. Nucl Eng Des 2010;240:2088–95.
- [52] Tang L, Zeng M, Wang Q. Experimental and numerical investigation on air-side performance of fin-and-tube heat exchangers with various fin patterns. Exp Therm Fluid Sci 2009:33:818–27.
- [53] Ebrahimi K, Jones GF, Fleischer AS. A review of data center cooling technology, operating conditions and the corresponding low-grade waste heat recovery opportunities. Renew Sustain Energy Rev 2014;31:622–38.
- [54] ASHRAE Technical Committee 9.9. Thermal Guidelines for Data Processing Environments, 4th ed. . Atlanta: W. Stephen Comstock,, 2015.
- [55] C.H. Hoang, M. Tradat, Y. Manaserh, B. Ramakrisnan, S. Rangarajan, Y. Hadad, et al. Liquid Cooling Utilizing a Hybrid Microchannel/Multi-Jet Heat Sink: A Component Level Study of Commercial Product. ASME 2020 International Technical Conference and Exhibition on Packaging and Integration of Electronic

- and Photonic Microsystems. American Society of Mechanical Engineers Digital Collection 2020.
- [56] Zhang K, Zhang X, Li S, Jin X. Experimental study on the characteristics of supply air for UFAD system with perforated tiles. Energy Build 2014;80:1–6.
- [57] Elger DF, LeBret BA, Crowe CT, Roberson JA. Engineering fluid mechanics. John Wiley & Sons; 2020.
- [58] Tradat M. Transient and Steady Experimental and Numerical Thermal Studies towards Energy Efficiency Improvements in Data Centers. Ph D Thesis. 2019.
- [59] Patankar SV. Airflow and cooling in a data center. J Heat Transfer 2010;132.
- [60] Brady GA, Kapur N, Summers JL, Thompson HM. A case study and critical assessment in calculating power usage effectiveness for a data centre. Energy Convers Manage 2013;76:155–61.
- [61] Yuventi J, Mehdizadeh R. A critical analysis of power usage effectiveness and its use in communicating data center energy consumption. Energy Build 2013;64: 90-4
- [62] Haywood A, Sherbeck J, Phelan P, Varsamopoulos G, Gupta SK. Thermodynamic feasibility of harvesting data center waste heat to drive an absorption chiller. Energy Convers Manage 2012;58:26–34.
- [63] Li Y, Wang S, Duan X, Liu S, Liu J, Hu S. Multi-objective energy management for Atkinson cycle engine and series hybrid electric vehicle based on evolutionary NSGA-II algorithm using digital twins. Energy Convers Manage 2021;230:113788.
- [64] Patel CD, Bash CE, Belady C, Stahl L, Sullivan D. Computational fluid dynamics modeling of high compute density data centers to assure system inlet air specifications. Proceedings of IPACK2001. pp. 8-13.
- [65] Zhang X, VanGilder JW, Jyengar M, Schmidt RR. Effect of rack modeling detail on the numerical results of a data center test cell. 2008 11th Intersociety Conference on Thermal and Thermomechanical Phenomena in Electronic Systems. IEEE2008. pp. 1183-90.